Influence of hydrogen on the microstructure and fracture toughness of friction stir welded plates of API 5L X80 pipeline steel

J.J. Hoyos[1,2]; M. Masoumi[3]; V.F. Pereira[4]; A.P. Tschiptschin[5]; M.T.P. Paes[6]; J.A. Avila[7]*

1. State University of Ponta Grossa, UEPG, Ponta Grossa, PR, Brazil.
2. Brazilian Nanotechnology National Laboratory, LNNano, Brazilian Center for Research in Energy and Materials, Campinas, SP, Brazil.
3. Center for Engineering, Modeling and Applied Social Sciences (CECS), Universidade Federal do ABC (UFABC), Santo André, SP, Brazil
4. State University of Campinas, UNICAMP, Campinas, SP, Brazil.
5. Metallurgical and Materials Engineering, University of São Paulo, USP, São Paulo, SP, Brazil.
6. Petrobras, CENPES, Rio de Janeiro, RJ, Brazil
7. UNESP – São Paulo State University, São João da Boa Vista, SP, Brazil

*Corresponding author: Prof. Dr. Julian A. Avila D. julian.avila@unesp.br, +55 19 36382432, Av. Profª Isette Corrêa Fontão, 505, Jardim das Flores, 13876-750 - São João da Boa Vista, SP, Brazil

- **Short title:** Hydrogen effects on FSWelded plates of an X80-pipeline steel.
- **Declarations of interest:** none

Abstract

In this work, the influence of hydrogen on the microstructure and fracture toughness of API 5L X80 high strength pipeline steel welded by friction stir welding was assessed. Samples were hydrogenated at room temperature for a duration of 10 h in a solution of 0.1M H_2SO_4 + 10 mg L^{-1} As_2O_3, with an intensity current of 20 mA cm^{-2}. Fracture toughness tests were performed at 0 °C in single edged notched bending samples, using the Critical Crack Tip Opening Displacement (CTOD) parameter. Notches were positioned in different regions within the joint, such as the stir zone, hard zone, and base material. Hydrogen induces internal stress between bainite packets and ferrite plates within bainite packets. In addition, hydrogen acted as a reducer of the strain capacity of the three zones. The base metal had moderate capacity to resist stable crack growth, displaying a ductile fracture mechanism. While the hard zone showed a brittle behavior with CTOD values below the acceptance limits for pipeline design (0.1 – 0.2 mm). The fracture toughness of the stir zone is higher than that of the base metal. Nevertheless, the stir zone displayed higher data dispersion due to its high inhomogeneity. Hence, it can also show a brittle behavior with critical CTOD values.

Keywords: friction stir welding; ISO 3183 X80M; high strength steel; hydrogen embrittlement.

1. Introduction

Friction Stir Welding (FSW) is a solid-state joining process, which eliminates the melting and solidification problems associated to the use of fusion welding process on high strength steels. Therefore, several efforts have been made during the past years for the successful implementation of FSW on these steels, which are used in energy, nuclear, petrochemical and building industries [1–8].

FSW does not significantly increase the hydrogen content in API 5 L X80 high strength pipeline steel during dry and underwater welding [1,9]. This suggests that FSW reduces the risk of hydrogen embrittlement in comparison to fusion welding processes during welding. This has been associated with the absence of hydrogen sources such as filler metal and process temperatures below the melting point.

Nevertheless, the validation of FSW also requires assuring the mechanical properties under hydrogen effects. As it is well known, hydrogen input could also take place during service conditions (cathodic charging or corrosive environments) [10]. After the hydrogen diffusion, atoms can get positioned at the lattice and crystal imperfections or traps, such as inclusions, voids, grain boundaries and dislocations [11]. This reduces the mechanical properties of steels, leading to hydrogen embrittlement [12,13].

The influence of hydrogen on the microstructure and mechanical behavior of high strength pipeline steels [14–20] and their welded joints [21–24] have been widely studied. For pipeline steels, the influence of the hydrogen in the yield strength and tensile strength cannot be deemed significant [14,15,25,26]. Nevertheless, the ductility (fracture elongation) [14,27,28] and fracture toughness decrease significantly in hydrogen environments [9,12,14–24,29]. In addition, the loss of ductility increases when the strength level of the steel is high [14,27]. Hydrogen induces the fracture mechanism transition from ductile to brittle, from microvoids coalescence to transgranular cleavage or intergranular fracture, respectively [17,28,30,31]. The detrimental effect of hydrogen is basically associated to the reduction of strain capacity of the matrix [32], which is usually a mixed ferrite-perlite or ferrite-bainite microstructure [21].

A similar trend is observed in welded joints of pipeline steels. For API 5L X70 and X52 pipeline steels, Chatzidouros et al [21] showed that fracture toughness of base metal (BM) and heat affected zone metal (HAZ) decreased after hydrogen cathodic charging. Lee et al. [22] showed that electrochemical hydrogen charging reduced the impact toughness of BM and coarse-grained HAZ at room temperature and -40 °C in API 5L X70 welded by shielded metal arc welding. An et al. [24] showed that hydrogen gas decreased the ductility (elongation and area reduction) and fracture toughness of BM and weld metal (spiral submerged arc welding), and had little influence in the yield strength and tensile strength of API 5L X80 steel. In addition, they showed that hydrogen increased the fatigue crack growth rate of the BM and weld metal.

As fusion welding processes result in a wide variety of microstructures, the influence of hydrogen in the mechanical behavior is attributed to several factors. On one hand, failure is affected by local hydrogen concentration, which depends on the binding energy traps. The low binding energy traps, grain boundaries and dislocations, are considered as the mains sources for hydrogen embrittlement [22]. On the other hand, some microstructures are proven more susceptible to hydrogen embrittlement such as coarse microstructures of welding joints [22], inclusions, and hard constituents of bainite and martensite/austenite (M/A) [16,21,24,33].

Few studies have reported the hydrogen effects on fracture toughness on FSW welded joints of pipeline steels [9,29]. The hydrogen decreased the ductility (elongation at fracture) of both the BM and stir zone (SZ) [9] and accelerated fatigue crack growth rate of the BM, SZ and HAZ [29]. Sun and Fujii [9], showed that the SZ showed higher resistance to hydrogen embrittlement than the BM. By contrary, Ronevich et al. [29], showed that the fatigue crack growth rate was slightly highest in SZ.

Although the FSW welded joint contains a hard zone (HZ), which is considered as a local brittle zone [4,34], there is no information reporting its behavior under hydrogen effects. This is important since the hydrogen would have a strong influence on this zone in comparison to the BM, restricting the commercial pipeline applications.

The current work examines the influence of hydrogen on fracture toughness of welded joints of API 5L X80 pipeline steel (ISO 3183 X80M). Chemical composition (0.04 %wt. C, 0.32 %wt. Si, 1.56 %wt. Mn, 0.06 %wt. Cr), microstructure (stir and hard zone with granular bainite, acicular ferrite, and bainite packets with irregular and straight ferrite plates) and mechanical properties (yield strength of 593 ± 21 MPa, ultimate strength of 658 ± 34 MPA and elongation of 17 ± 1 %) were reported in previous work [2]. Fracture toughness was measured at 0 °C using CTOD with notches placed in different regions within the joint. The results suggest that FSW has a limited applicability under hydrogen effects since CTOD values of the hard zone are below the acceptance limits, 0.1-0.2 mm, for pipeline design or defect acceptation [4].

2. Experimental procedure

2.1 Welding procedure: friction stir welded joint

Plates of API 5L X80 pipeline steel of 450 mm x 95 mm x 9.5 mm were joined by FSW in the normal direction of the original plate rolling direction. The FSW tool made of polycrystalline cubic boron nitride reinforced with tungsten-rhenium (PCBN-WRe) had a probe of 9.5 mm and a shoulder diameter of 20 mm. The FSW parameters were: spindle speed of 300 rpm, travel speed of 100 mm/min and axial force of 34 KN. These parameters were selected from previous works [2,5].

2.2 Hydrogen charging and measurements

Hydrogen charging was made in the three-point bend single edge notched (SENB) samples (Figure 1a). The SENB samples dimensions were based on the ASTM 1820 standard [35] proportions, BxWx4.5W = 9.5x19x85.5 mm^3, where B is the thickness and W is the width. Notches were located parallel to the welding and rolling direction through the SZ, HZ and BM.

For CTOD experiments, SENB samples were hydrogenated during 10 h at room temperature in a solution of 0.1M H_2SO_4 + 10mg L^{-1} As_2O_3, with an intensity current of 20 mA cm^{-2}, and immediately stored in liquid nitrogen bath. The solution and intensity current were chosen from previous work in duplex (austenitic-ferritic) stainless steels[36]. In addition, SENB hydrogen (H)-charged samples were degassed during 45 min at 0 °C, in order to evaluate the hydrogen fugacity during CTOD experiments. This time is higher than that used in the fracture toughness tests.

The charging time of 10 h was chosen from preliminary experiments. For this, rectangular blanks with dimensions of 20 mm x 9.5 mm x 3 mm were cut from the welded joints (Figure 1b and 1c) and hydrogenated for 1, 10 and 100 h. The hydrogen content was measured by the hot extraction method at 400 °C (diffusible) and 900 °C (non-diffusible or residual) for 40 min. The detection limit of the equipment is 5 x 10^{-2} ml H_2/100g, and the resolution is 1 x 10^{-2} ml H_2/100g. Prior to measurements, the equipment was calibrated with four volumes of low hydrogen and with four repetitions for each run.

As can be seen in Figure 2, the hydrogen had a high diffusivity in BM rectangular blanks, reaching 90 % of maximum diffusible hydrogen after 1 h of hydrogen charging. The diffusible hydrogen increased from 3.28 to 3.32 ml H_2/100 g when the hydrogen exposure time increased from 10 to 100 h (around 1 %). Therefore, it is considered that full hydrogen saturation was reached after 10 h. According to Escobar et al [37] this kind of steels reaches the complete hydrogen saturation after lower times.

During aging at room temperature for 10, 20 and 60 min, the initial diffusible hydrogen was reduced to 70, 50 and 30 %. This confirms that the hydrogen present in the steel is mainly diffusible hydrogen. It is worth note that the hydrogen pickup of the BM is higher than that in the welded joint (SZ and HZ rectangular blanks). The BM had a higher capacity than SZ for hydrogen absorption [9]. On the other hand, the change in residual hydrogen cannot be deemed significant. It is around 0.5 ± 0.2 ml H_2/100 g for most samples. This indicates that H-charging increased mainly the diffusible hydrogen.

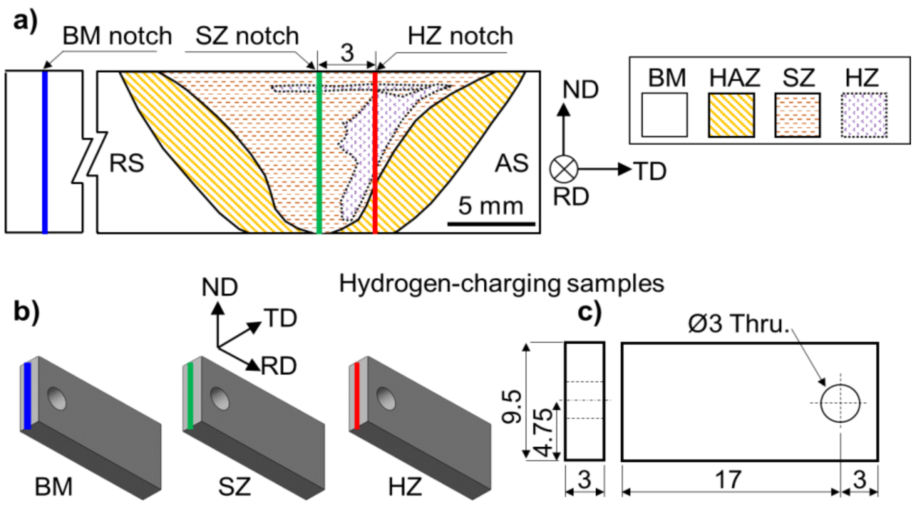

Figure 1. *a) cross-section view of the welded joint containing the through-thickness notch locations of the fracture toughness tests; b) 3D H-charged samples: geometry and c) dimensions in mm. RD: Rolling direction, ND: Normal direction, TD: Transverse direction, AS: Advancing side, RS: Retreating side.*

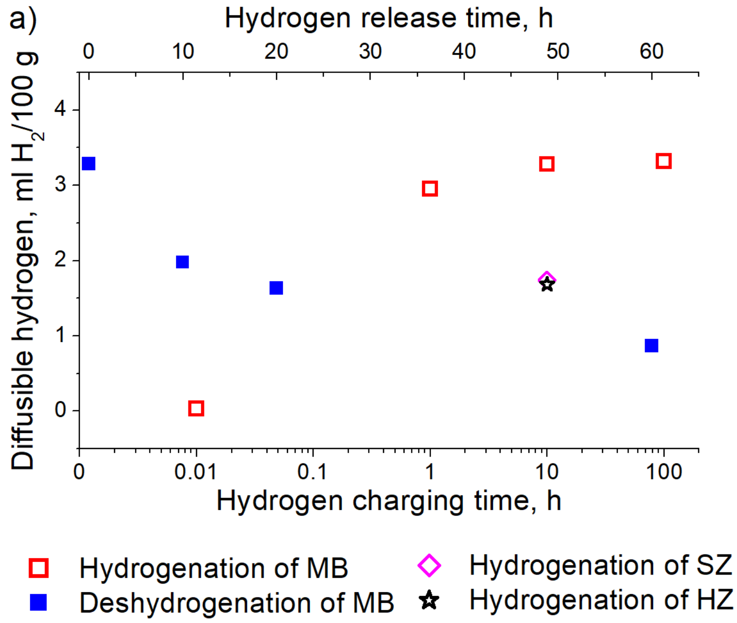

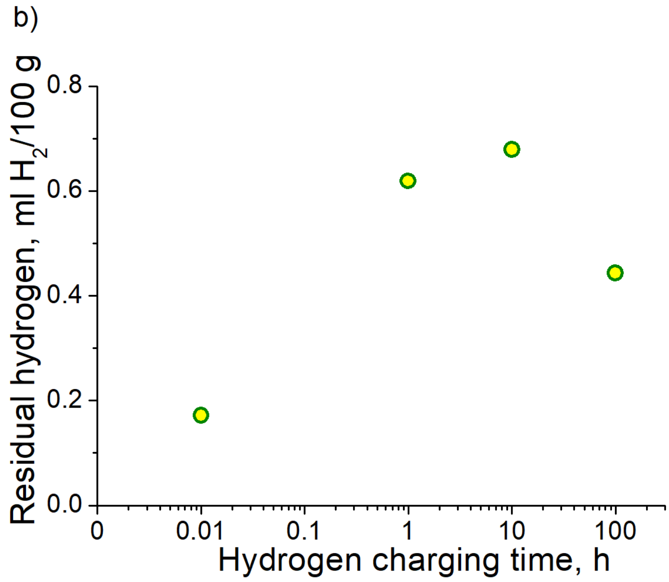

Figure 2. a) Diffusible and b) residual hydrogen content of rectangular blanks.

2.3 Fracture toughness assessment

The CTOD test is intended to measure the fracture toughness by applying a monotonic and increasing load, simulating a quasi-static load. For this, SENB samples were taken from the welded plates and BM. The CTOD parameter was chosen to assess fracture toughness due to the plastic behavior of the FSW joint in this steel [2]. Before CTOD tests, the samples were subjected to local compression using the B-type device according to the ISO 15653:2010 standard [38]. Then, a fatigue precracking was conducted on the machined notches at room temperature, with force ratio of 0.5 and frequency of 40 Hz until the total size of the crack reaches approximately 10.45 mm (0.55xW).

After precraking, side grooves with a depth of 10 % B at both sides of the samples were machined, as recommended by the ASTM-E 1820 standard [35]. Furthermore, the testing procedure, CTOD calculation, validation of the data and fracture front straightness criteria followed the ASTM-E1820 standard recommendations [35]. The CTOD tests were conducted on SENB H-charged samples at 0° C, with at least three repetitions for each microstructural selected zone, BM, SZ, and HZ.

2.4 Metallographic characterization and fracture surface analysis

After finishing the CTOD tests, the SENB samples were broken in two halves exposing the fracture surfaces. Hence, fracture surfaces were covered with a protection film. One half was used to study the fracture surface and the other was sectioned to identify the microstructure involved in the crack propagation, as recommended by BS EN

ISO 15653:2010 standard [38]. During the SEM analysis, these samples had their surfaces cleaned using an ultrasonic water bath for 10 min in acetone.

The metallographic samples were ground and polished using conventional methods, sample surface was manually polished with sandpaper and diamond polishers. The final polishing stage was carried out using colloidal silica. No etching procedure was conducted before the acquisition of electron backscatter diffraction (EBSD) maps. Images of the fracture surfaces and EBSD maps were acquired using light optical microscopy and scanning electronic microscopy with an EBSD system. Measurements at the SEM were conducted using beam energy of 20 KV and a step size of 0.5 µm.

From the surface fracture analysis, the tests were validated according to the ASTM E1820 standard [35], where the fatigue crack straightness met the requirement and, crack size and width ratio (a/W) was approximately 0.58 for all tests, which is between the suggested by the ($0.45 \leq a/W \leq 0.75$).

The localized plastic strain using the EBSD data in two distinct areas of the BM and SZ was calculated from the lattice curvature (or steep boundaries), as a statistical misorientation quantification as called Kernel average misorientation (KAM) technique [39,40]. This was made by means of the average point-to-point misorientation angle within the third neighbor pixel with a threshold angle of 5° to avoid grain boundary effects.

Furthermore, the influence of coincidence site lattice (CSL) boundaries on crack propagation was investigated in detail. Despite having crystallographic misorientation between two adjacent lattices at CSLs, they have low energy because of good atomic fit. CSL boundaries were identified according to the grain boundary direction and a certain rotation angle (i.e., $\Sigma3=60°\langle111\rangle$ describes as 60° rotation around <111> direction).

3. Results

3.1 Hydrogen content measurements

The diffusible hydrogen of SENB samples was 2.55 ml H_2/100g after cathodic charging for 10 h, and 1.67 ml H_2/100g after hydrogen charging and aging during 45 min at 0 °C. This suggests a slight decrease of hydrogen during the CTOD testing. In these samples, the hydrogen discharging is lower than that in BM rectangular blanks (Figure 2) since the aging was made at a lower temperature and the thickness was higher. In this steel, the loss of hydrogen occurs slower when the thickness is increased. The probability per unit of time of successful desorption of a hydrogen atom from a specific trap is inversely proportional to the thickness [37].

3.2 Fracture Toughness

Figure 3 shows the Force – crack mouth opening displacement (CMOD) of the samples with the lowest toughness of each condition, BM, SZ, and HZ. During the test, a clip-on-gage measures the CMOD. The test finishes when the crack reaches an unstable growth stage. Samples with notches located at BM and HZ display the highest and lowest areas below the curve, respectively. This indicates that BM has the highest capacity to resist stable crack growth, and consequently the highest fracture toughness. While HZ sample displays the lowest fracture toughness. The fracture toughness is higher when the area below the Force–CMOD curve is increased.

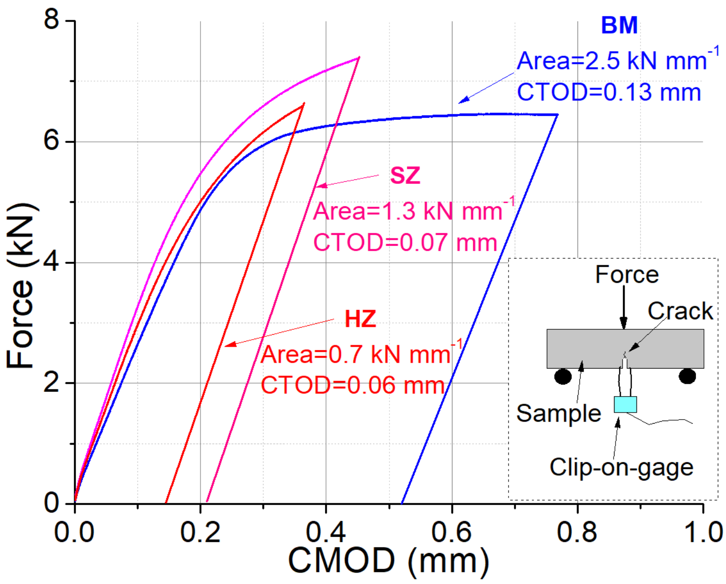

Figure 2. *Load-CMOD curves, CTOD test scheme, area under the curve and calculated CTOD results of the H-charged samples. Notches located at: a) BM, b) SZ and c) HZ.*

Figure 3 depicted CTOD results for SENB H-charged samples. The samples with notches located at the BM and SZ show mostly CTOD values higher than 0.20 mm with steady load-CMOD curves and large plastic deformation. However, there are some outliers with CTOD values of 0.13 mm and 0.07 mm respectively, which were associated with material inhomogeneity due to the FSW deformation and thermal cycle. Samples with notches located at the HZ showed a steady behavior, mostly brittle with little plastic deformation before failure, and values below the acceptance limits, 0.1 to 0.2 mm for pipeline design or defect acceptation [41].

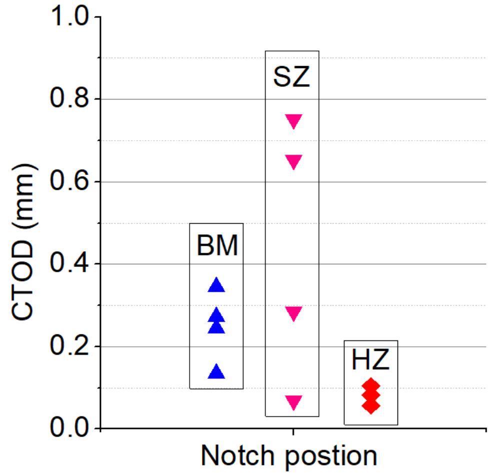

Figure 3. *CTOD summary in SENB H-charged samples tested at 0 °C.*

3.3 Fractography and metallography analysis

After finishing the CTOD test, the samples were separated in two halves to conduct the fracture surface analyses, as indicated elsewhere [38,42]. Figure 4 shows fracture surfaces of samples with highest and lowest toughness values from each one of the assessed conditions. From a macro view of fracture surfaces it is difficult to distinguish the size of the regions. However, some remarks can be pointed out.

For all samples, the crack propagation direction is upwards. Three regions can be identified: fatigue precracking region, crack propagation during CTOD test, and fatigue-crack marking. Before the fatigue marking, the CTOD test finished. Then, the samples were submerged in liquid nitrogen and broken by impact, resulting in a cleavage surface. These regions do not make part of the crack produced during the CTOD test, thus, is dismissed from the current analysis. It is worth noting that grooves side machining removed some microstructures depicted in Figure 1, mainly the HAZ at the HZ. However, it was not enough to cause a plane crack front propagation during the CTOD tests.

During the CTOD test, several fracture mechanisms can act within the crack propagation region, starting with a stretch of the crack tip during the blunting, thereafter a ductile tearing and a fast-final fracture, usually showing cleavage features.

Samples with high CTOD values (above 0.10) depicted a large stable crack propagation region (Figure 4a, 5b, and 5c). The BM fracture surfaces are similar despite the difference in CTOD values. Thus, the crack propagation presented a straight and proportional path of approximately 1 mm. While the crack surface at the SZ sample of high CTOD presented a regular straight front like BM samples.

On the other hand, samples presenting low CTOD (Figure 4d, 5e, and 5f) displayed a larger and more irregular crack front than BM sample. This result agrees with the little plastic deformation observed for lowest toughness samples at the load-CMOD curves in Figure 2. The fracture toughness is lower when the crack propagation is easier. For the samples with CTOD values below 0.10, the crack propagation extension was higher in the bead side than in the root side of the welded joint. Short crack propagation into a plastic regime can be explained by the crack arrest delivered by the refined microstructure found in the root side [36]. While the large crack extension into a brittle fashion can be explained by the high hardness values and large bainitic packets found close to the bead side, which was proved to present low toughness in the hydrogen (H)-free samples [2].

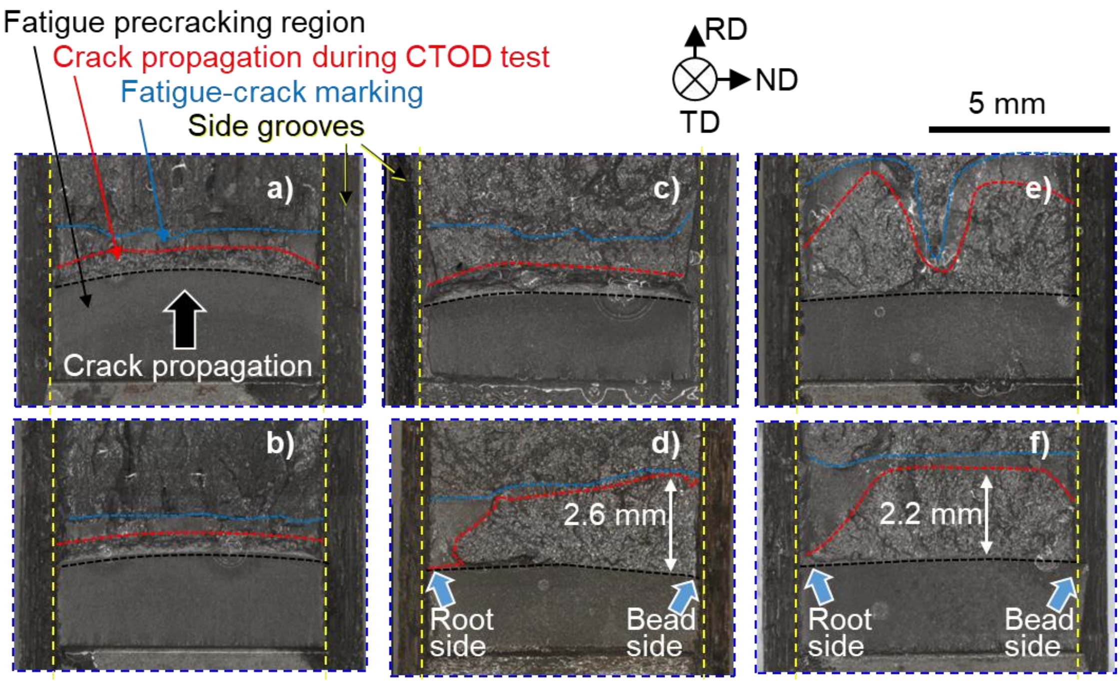

Figure 4. *Fracture surfaces showing the fatigue precracking, crack propagation during the CTOD test and fatigue-crack marking after the CTOD test at: BM samples with CTOD of a) 0.35 mm and b) 0.13 mm, SZ samples with CTOD of c) 0.75 mm and d) 0,07 mm, HZ samples with CTOD of e) 0.10mm and f)0.06 mm. Tests conducted at 0°C.*

Figure 6 shows a zoomed-in view of the fracture surface for the samples with the lowest CTOD values of each one of the assessed conditions. This allows focusing on the start and cracking propagation region. Four zones can be identified: the stretch zone wide (SZW), ductile tearing (DT), cleavage fracture (CL) start and growth, and start of the fatigue marking (FM). Their size and distribution could be correlated with the Force-

CMOD curve, where larger areas or energy expended during the crack tip blunting and propagation, delivered higher CTOD values.

The SZW of the BM, SZ and HZ seems to be higher than 20 µm, however it is difficult to state a value due to the low magnification images. After the SZW, the BM shows a large ductile tearing (500 µm), showing mostly a propagation mechanism composed by large and small dimples (Figure 5a). The crack propagation at the SZ sample, shown in Figure 5f, presented mostly CL crack propagation after the SZW. Furthermore, the crack propagation was arrested close to the root side, because the refined microstructure reported in the bottom of this welds [36]. After the CTOD, the fatigue marking procedure follows the SZW, as observed in fatigue striation morphology in Figure 5g. In addition, Figure 5h and 6i show the position of cleavage initiators. These initiators were identified as M/A microconstituents from previous microstructural characterization [2]. The fracture mechanism at HZ, shown in Figure 5l - 6o, is similar to the SZ described mechanism.

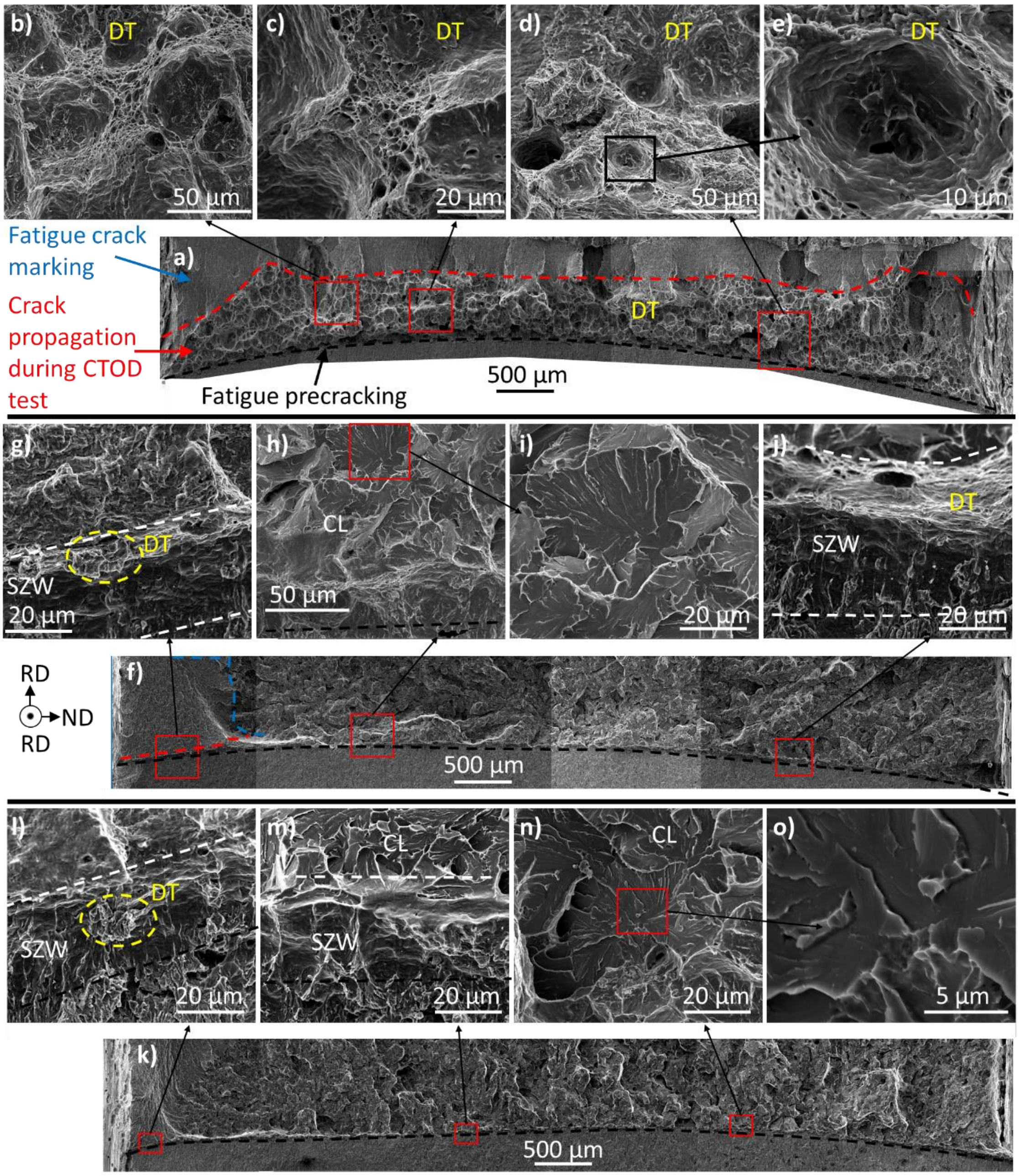

Figure 5. *Crack propagation region during the CTOD test of the lowest toughness results. Same reported in Figure 4. BM: a)-e), SZ: f)-j) and HZ: k)-o). Left side of f) and k) shows the root of the welding pass. Tests conducted at 0°C. Also, the stretch zone wide (SZW), ductile tearing (DT), and cleavage fracture (CL) can be observed.*

Figure 6 shows the EBSD analysis of fracture surface for the samples with lowest toughness. This allows identifying the microstructures involved in the crack propagation. Detailed zoom-in images show the end of the fatigue precracking (FP), the stretch zone wide (SZW) and high, ductile tearing (DT), and the cleavage fracture (CL) start and propagation. In addition, secondary cracks were highlighted (maps).

The crack propagation paths start from the fatigue pre-cracked (FP) tip, followed by the crack propagation conducted during the CTOD test, which is composed first by a stretch zone and follow by a ductile tearing, and finally occur the cleavage propagation featured by the presence of facets. Due to the plastic zone produced around the crack tip, several cracks nucleate ahead of this point, but only initiated cracks align with the main stresses will connect and create a macrocrack, and some others will remain as secondary cracks alongside the main crack propagation path.

In the first stage of the crack propagation, the tip becomes round due to the blunting caused by the applied force that consequently originated a stretch of the crack tip. These stretch zones present a geometry like a concave parabola with half of the parabola in each half of the sample, represented by the width (SZW) and height dimensions. Twice the height, measured tilting the crack tip 45° as explained in a previous research [43], must be equal to the experimental measurement of CTOD. Their sizes depend on the amount of energy they can accumulate in the form of plastic deformation before starting stable crack propagation. Therefore, a stretch zone can be observed much larger at the BM (around 300 µm) than SZ (around 80 µm) and HZ (around 20 µm). However, a high deformed material produces low indexing quality, as shown in Figure 6b.

Although the hydrogen caused an embrittlement due to its presence within the matrix, the BM offered a better crack arrest than other conditions. This is related to its refined microstructure and lower hardness [2]. On the other hand, both SZ and HZ presents a small blunting stage with a short SZW, and short ductile tearing (less than 20 µm). Note that the SZW is higher at the SZ than HZ, which coincides with the CTOD values. After this small stage of stable crack propagation on the SZ and HZ, cleavage facets can be observed in the crack path.

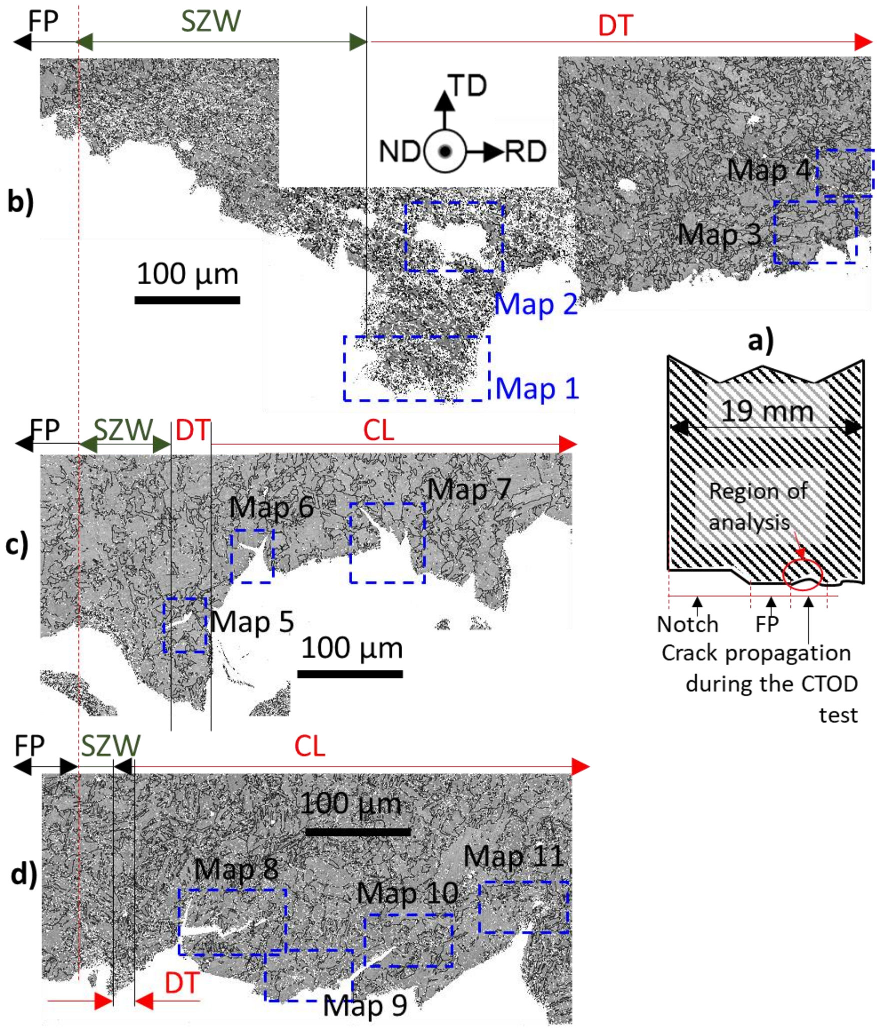

Figure 6. *Microstructure identification of the crack propagation path during the CTOD test of the lowest toughness samples, a) schematic of the transversal cut showing the machined notch, fatigue precracking (FP) path, crack propagation during the CTOD test and analysis region zoomed-in in b) BM, c) SZ and d) HZ. Secondary cracks were highlighted with dashed rectangles.*

Figure 8 shows the crystallography orientation maps showing the propagation of secondary cracks next to the main crack. From previous work [2], the microstructural characterization indicated that the three zones contained granular bainite, acicular ferrite, and bainite packets with irregular and straight ferrite plates. Cracks started in the grain boundaries and propagated in a transgranular way in all conditions. However, for SZ and HZ, with large bainite packets and little change in crystallography orientation within packets, cracks are straight and go throughout the packets. Consequently, facet cleavage was observed. EBSD data were not submitted to a cleanup postprocessing procedure to represent the lack of indexable diffraction pattern in the deformed regions. Likewise, low indexing has been reported to appear in highly deformed and fine-grained material [44]. Figure 7h-8k from SZ and Figure 7e-8g from HZ, shows low indexing quality between bainite packets and ferrite plates within bainite packets, noticed as lack of indexing pixels (white pixels) within the maps. Then, deformation of the matrix caused by the H-charging can be associated to the not indexed places, e.g., the matrix of the secondary cracks of the SZ and HZ condition. This fact is related to the hydrogen penetration within the matrix, which deformed the matrix and prevented the formation of Kikuchi patterns during EBSD measurements, therefore avoiding its crystallography identification.

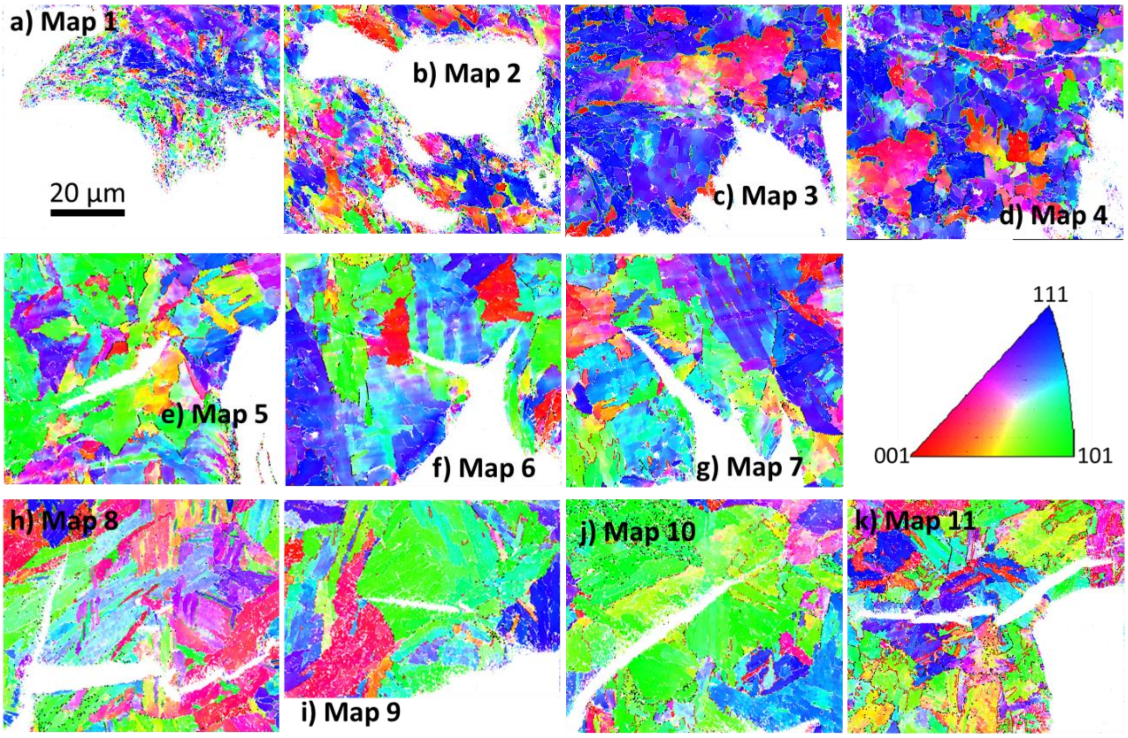

Figure 7. Orientation maps showing secondary cracks alongside the main crack propagation a)-d) BM, e)-g) SZ and h)-k) HZ. Maps were not submitted to the clean postprocessing procedure.

Fracture toughness was higher in BM despite having higher diffusible hydrogen. The formation of ultrafine grains (less than 1 µm) surrounded the microstructural defects in the BM might explain the higher fracture toughness. Furthermore, the development of the local orientation analysis of spatial crystallographic texture around secondary cracks generated from crack-tip plastic zone was investigated in detail, to provide an explanation of higher resistance to hydrogen-induced cracking of the BM.

Figure 8 shows the Kernel average misorientation map in two distinct areas of the BM and SZ (map 1 and 7). Note, deformation was associate with the presence of green lines and less deformed with the blue matrix. The BM shows higher ratio between green lines and blue matrix. Hence, BM has higher deformation than SZ. This coincides with the ductile tearing features of the BM and the little plastic deformation of the SZ. In addition, localized concentrate deformation was found in the crack vicinity of the BM.

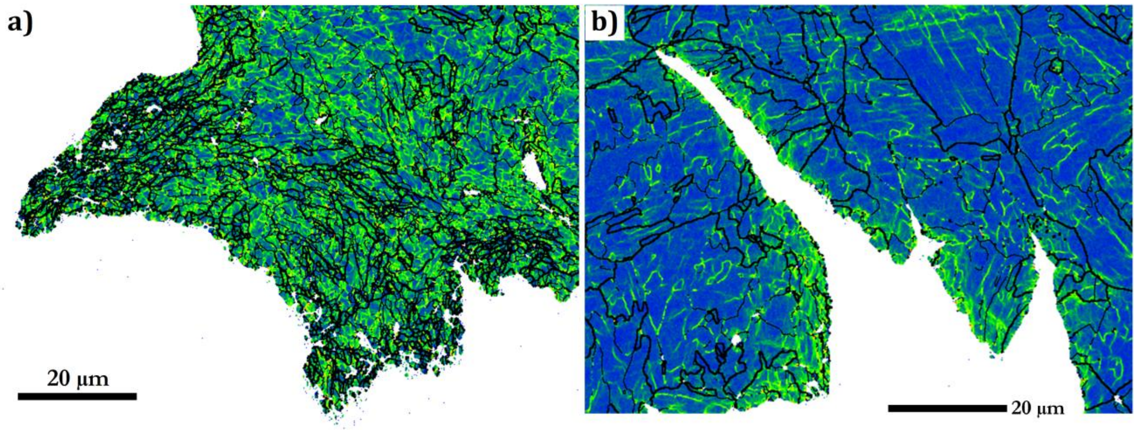

Figure 8. Kernel average misorientation map (a) map 1 and (b) map 7.

Figure 9 presents the variation of boundary types according to its misorientation in the BM, SZ and HZ. For all regions, grains with misorientation angles less than 5 degrees were predominant. The least fraction of these grains belonged to BM zone. Hence, the severe plastic deformation and high temperature during FSW induced the formation of new strain-free recrystallized grains in SZ and HZ. By contrary, BM zone shows the highest fraction of grain boundaries between 15° and 45° since it was not affected by welding process [45]. While the variation of boundaries with misorientation angles above 45° cannot be deemed significant. These boundaries correspond to bainite packets boundaries [2]. Although Zajac et al. [45] also showed the presence of misorientation angles distribution between 50° and 60° belonged to lower bainite, no significant variation was found in three distinct areas.

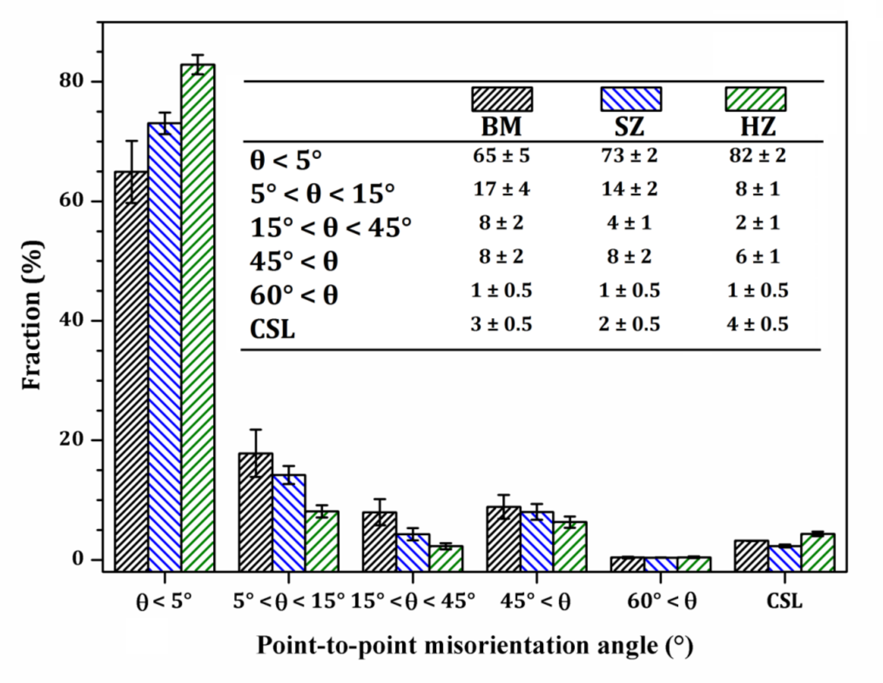

Figure 9. Distribution of boundary types of investigated samples.

Figure 10 shows the distribution of CSL boundaries of three investigated regions. The fraction of Σ3 boundaries is highest in BM than in SZ and HZ. Σ3 boundaries are known as twin boundaries which are expected to improve the toughness due to prevention of microcracks initiation and propagation [46]. However, Eskandari et al. [47] and Mohtadi-Bonab et al. [48] reported that true single or multiple twining could not be created in a low carbon pipeline steels because of the higher stacking fault energy (SFE). Therefore, the Σ3 boundaries act as high angle grain boundaries and might be providing an easy path for the intergranular crack propagation. Analyzing the other special boundaries, it is concluded that the number of CSLs such as Σ11 (50.47°<110>), Σ13b (22.79°<111>), and Σ19a (46.8°<111>) are highest in the HZ and SZ samples. While the portion of Σ25a (16.26°<100>) was highest at the BM sample. Boundary associated with close-packed direction with small lattice mismatch exhibits more resistance to crack propagation. In body-centered cubic (BCC) materials, <111> direction is a more compact atomic arrangement than <110>. Therefore, SZ and HZ should provide a higher crack resistance than BM. Nevertheless, the variation of CSL boundary distributions is negligible, and thus, there is no influence on the fracture toughness.

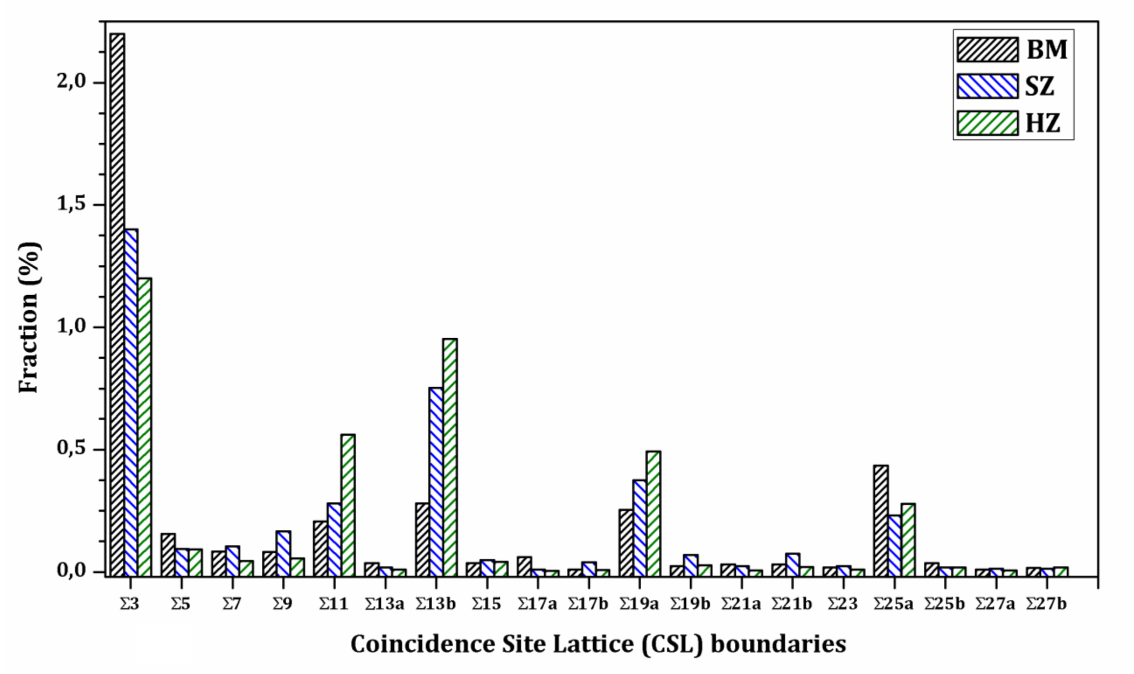

Figure 10. Distribution of special CSL boundaries.

Figure 11 shows the orientation distribution function estimated from each EBSD data at constant $\varphi_2 = 45°$ which presents the main texture components. Thereby, the grain orientation was expressed according to the (hkl)[uvw] term which (hkl) plane perpendicular to the crystal plane of the normal direction (ND) and [uvw] direction is parallel to the direction of the welding direction (WD). The {112} and {111}//ND grains (i.e.,$(112)[02\bar{1}], (111)[10\bar{1}], (111)[\bar{2}11], (112)[\bar{2}01], \text{and } (112)[1\bar{1}0]$ components) were identified in BM area. While, mainly {110}//ND grains were developed in the SZ and HZ samples.

Abraham et al. [49] reported the presence of hydrogen reduces dislocation-dislocation interactions, accelerating planar slip since the slip and long-range strain fields introduced by dislocations piles-up creates shear stress along the slip plane and increase localized stress distribution around the crack tip to enhance crack propagation. Therefore, the formation of individual slip line, corresponding to {110}-planes facilitates crack propagation at the HZ and SZ.

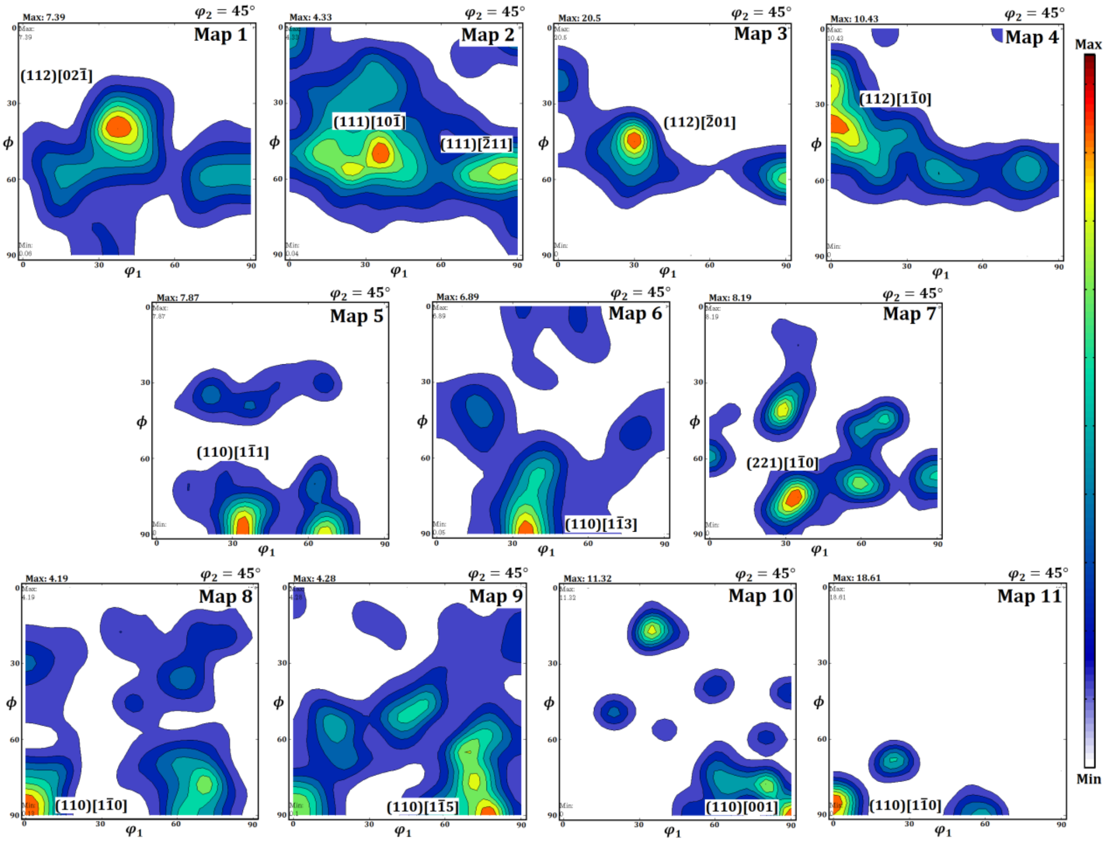

Figure 11. Orientation distribution function at constant $\varphi_2 = 45°$ of all specimens.

Discussion

The influence of hydrogen in fracture toughness

In comparison to similar H-free samples tested also in 0 °C [2], the H-charged samples presented lower fracture toughness. For samples with notches located at the BM, SZ and HZ, the average fracture toughness decreased from 0.96 to 0.25 mm, 0.48 to 0.43 mm, and 0.22 to 0.08 mm, respectively. This suggests that SZ had higher resistance to hydrogen embrittlement than BM, which is in according with the results reported by Sun and Fujii [9]. Nevertheless, samples with notches located at SZ displayed higher data dispersion under hydrogen effects. Therefore, a complementary analysis requires the comparison of the lowest fracture toughness of each condition. This comparison indicates that the fracture toughness decreased from 0.94 to 0.13 mm, 0.39 to 0.07 mm, and 0.19 to 0.06 mm for samples with notches located at BM, SZ and HZ samples, respectively. Therefore, hydrogen charging reduced significantly the fracture toughness of both BM and FSW welded joints, which coincides with the results reported by Ronevich et al [29]. Moreover, after hydrogen charging, samples with notches located at HZ and SZ reached CTOD values below the acceptance limits (0.1 to 0.2 mm) for pipeline design or defect acceptation. This represent a main issue for the implementation of friction stir welded joints of high strength steels in hydrogen environments. Although FSW reduces the hydrogen pickup during welding in comparison to fusion welding processes [1,9], it did not reduce the risk of hydrogen embrittlement due to the formation of localized brittle zones. Hence, the influence of hydrogen in fracture toughness could be worse than that reported for conventional welding process [21,22,24,50].

On the other hand, H-charged samples with notches located at the SZ and HZ presented similar toughness values than H-free samples tested in -40 °C [2]. As low plastic deformation at the crack nucleation and large unstable crack propagation were observed in the H-charged samples, the influence of hydrogen is likely to shift the ductile-brittle transition temperature to a higher temperature in more than 40 °C. A similar trend was reported by Fassinas et al [51] for F22 and X65 steel with increases of the ductile-brittle transition temperature of 30 °C and 10 °C, respectively.

The influence of hydrogen in the microstructure

Although the SZ has higher mean fracture toughness than BM, the SZ displayed high data dispersion, reaching values of fracture toughness as low as the HZ. This behavior could be related to the distribution of low and moderate angle boundaries of these zones, and the formation of localized brittle zones. The fracture toughness is often controlled by the most brittle phase [22].

On one hand, BM displayed the highest proportion of low angle boundaries ($5° < \theta < 15°$). For low carbon pipeline steels (in the range of X100 to X120), Zajac et al. [45] reported that the high proportion of low angle boundaries of complex bainitic microstructures is due to the growth direction of the ferrite laths. Pak et al. [52] also explained that induced stress during bainitic transformation promotes the formation of the coarse plates of bainite by the coalescence of identically oriented individual platelets, which deteriorates the fracture toughness. In addition, Mohtadi-Bonab et al. [2] reported that the transgranular type of hydrogen induced cracking propagates at grains containing an accumulation of low angle grain boundaries due to the lack of fully recrystallization of ferritic X60 steel [48]. Therefore, an early premature fracture is expected in the BM due to having the highest portion of low angle boundaries.

On the other hand, the grain boundaries with considerable stored energy due to the misfit in the orientation of the two adjacent grains have different propagation behaviors ahead of crack. Grain boundaries can reduce propagation rate by providing barriers and deflection ahead of intergranular cracks, while they can also provide a preferred path for propagation of transgranular crack propagation [11,48,53]. Therefore, it is expected that the highest portion of moderate angle boundaries ($15^\circ < \theta < 45^\circ$), corresponding to bainite packets boundaries increased crack propagation resistance at the BM by providing more crystallographic barrier ahead of the crack tip.

Bhadeshia [54] documented that the boundaries between bainitic ferrite laths within a packet with misorientation less than 15° cannot hinder crack propagation. Whereas, boundaries between bainite packets (with misorientation greater than 15°), effectively impede crack propagation. Mao et al. [55] also confirmed that the bainite packet boundaries in low carbon steels act as a barrier for crack propagation, consequently, improves fracture toughness. Therefore, the fracture toughness of the BM should be higher than that of welded joint.

The inhomogeneity of the SZ could result in a change in the proportion of low and moderate angle boundaries, and the formation of localized brittle zones, leading to high data dispersion of the fracture toughness. This also explains the opposite results reported by Sun and Fujii [9] and Ronevich et al. [29].

In comparison to similar H-free samples tested also in 0 °C [2], the H-charged samples displayed a lower indexing quality. This indicates that hydrogen induces internal stress, especially between bainite packets and ferrite plates within bainite packets. In addition, hydrogen acted as a reducer of the strain capacity of the material, reducing the fracture toughness. Hydrogen effect seems to be worse in localized zones of the welded joint such as HZ, in which the hardening effect caused by the FSW process results in localized brittle zones such as hard constituents of M/A. This could be correlated with the hydrogen-enhanced localized plasticity (HELP) model [10,11,56]. The hydrogen in association with a hardened microstructure having much more dislocations than BM, as observed in the SZ and HZ, increases the local plasticity at the dislocations and facilitates the nucleation and propagation of cracks.

The ferrite and bainite observed in the BM, presented a ductile tearing fracture mechanism with a previous large stretch zone, also reported by Saleh et al. [57] in an X70 H-charged as slip-based cracking on a type of microstructure. However, samples with lowest fracture toughness of SZ and HZ presented a short stretch zone and crack propagation under cleavage mechanism, similar to that presented in coarse grained HAZ of H-charged arc welded joints [22]. Hence, the H-charged samples with microstructures composed of refined ferrite and bainite presented a larger capacity to arrest crack propagation than large bainite packages and harder microstructure found at the SZ and HZ. Other authors reported inclusions as cracks initiators [24,33]. However, it was not the case for the present research.

The difference in the crack blunting of BM and welded joint manifested in large or short stretch zones were well correlated to fracture toughness, where large stretch zones mean the high capacity to accommodate strain and deliver high CTOD values. Crack nucleation at SZ and HZ were located at the grain boundaries and martensite-austenite microconstituent, which is the same crack starting mechanism reported for H-free samples [24].

Conclusions

- Hydrogen reduces the fracture toughness of API X80 and its FSW welded joints. The hard zone of the welded joint shows the lowest fracture toughness with values below the acceptance limits for pipeline applications. On the other hand, the mean fracture toughness of the stir zone is higher than that of base metal. Nevertheless, the stir zone displays high data dispersion, reaching values as low as that of the hard zone. Therefore, FSW has a limited applicability under hydrogen-charging environments.
- The influence of hydrogen on the fracture toughness is related to the distribution of low and moderate angle boundaries of these zones, and the formation of localized brittle zones. The highest proportion of low angle boundaries in the base metal, and the highest proportion of moderate angle boundaries in the welded joint reduce the resistance to crack propagation. While the formation of localized brittle zones in the hard zone and stir zone promotes the cleavage mechanism.
- Further works about the influence of hydrogen in the welded joint, both hard and stir zone, are necessary. In the first place, the use of post welded heat treatments should be analyzed, in order to reduce the formation of localized brittle zones. Secondly, the fracture toughness should be evaluated under more conventional hydrogen environments, such as *in-situ* cathodic polarization simulating hydrogen charging of subsea equipment, to establish its influence on the mechanical behavior of FSW joints.

- **Acknowledgements**

The authors are grateful to the Company TenarisConfab for sample supply and PETROBRAS for the financial support. This study was financed in part by the National Council for Scientific and Technological Development, Brazil CNPq, processes 403530/2014-8 and 150215/2016-9. Research supported by LNNano - Brazilian Nanotechnology National Laboratory, CNPEM/MCTIC.

References

[1] J.J. Hoyos, V.F. Pereira, R.R. Giorjao, T.R. McNelley, A.J. Ramirez, Effect of friction stir welding on hydrogen content of ISO 3183 X80M steel, J. Manuf.

Process. 22 (2016) 82–89. doi:10.1016/j.jmapro.2016.01.012.

[2] J.A. Avila, J. Rodriguez, P.R. Mei, A.J. Ramirez, Microstructure and fracture toughness of multipass friction stir welded joints of API-5L-X80 steel plates, Mater. Sci. Eng. A. 673 (2016) 257–265. doi:10.1016/j.msea.2016.07.045.

[3] T.F.A. Santos, T.F.C.F.C.T.F. Hermenegildo, C.R.M.R.M.C.R.M. Afonso, R.R.R.R. Marinho, M.T.P.M.T.P. Paes, A.J.J.A.J. Ramirez, Fracture toughness of ISO 3183 X80M (API 5L X80) steel friction stir welds, Eng. Fract. Mech. 77 (2010) 2937–2945. doi:10.1016/j.engfracmech.2010.07.022.

[4] J.A. Ávila, C.O.F.T. Ruchert, P.R. Mei, R.R. Marinho, M.T.P. Paes, A.J. Ramirez, Fracture toughness assessment at different temperatures and regions within a friction stirred API 5L X80 steel welded plates, Eng. Fract. Mech. 147 (2015) 176–186. doi:10.1016/j.engfracmech.2015.08.006.

[5] J.A. Avila, E. Lucon, J.W. Sowards, P.R. Mei, A.J. Ramirez, Assessment of Ductile-to-Brittle Transition Behavior of Localized Microstructural Regions in a Friction-Stir Welded X80 Pipeline Steel with Miniaturized Charpy V-Notch Testing, Metall. Mater. Trans. A. 47 (2016) 2855–2865. doi:10.1007/s11661-016-3473-z.

[6] P. Xue, Y. Komizo, R. Ueji, H. Fujii, Enhanced mechanical properties in friction stir welded low alloy steel joints via structure refining, Mater. Sci. Eng. A. 606 (2014) 322–329. doi:10.1016/j.msea.2014.03.058.

[7] G.W. Young, Evaluation of Friction Stir Processing of Hy-80 Steel Under Wet and Dry Conditions, Naval Postgraduate School, 2012. http://www.dtic.mil/docs/citations/ADA561862.

[8] Norman E Overfield, Feasibility of underwater friction stir welding of hardenable alloy steel, Naval Postgraduate School, 2010. http://www.dtic.mil/dtic/tr/fulltext/u2/a536365.pdf.

[9] Y. Sun, H. Fujii, Improved resistance to hydrogen embrittlement of friction stir welded high carbon steel plates, Int. J. Hydrogen Energy. 40 (2015) 8219–8229. doi:10.1016/j.ijhydene.2015.04.070.

[10] D. François, A. Pineau, A. Zaoui, Chapter 7: Environment Assisted Cracking, in: Mech. Behav. Mater. Solid Mech. Its Appl., 1st ed., Springer Netherlands, Dordrecht, 2013: pp. 363–406. doi:10.1007/978-94-007-4930-6_7.

[11] E. Ohaeri, U. Eduok, J. Szpunar, Hydrogen related degradation in pipeline steel: A review, Int. J. Hydrogen Energy. 43 (2018) 14584–14617. doi:10.1016/j.ijhydene.2018.06.064.

[12] T. Depover, D. Pérez Escobar, E. Wallaert, Z. Zermout, K. Verbeken, Effect of hydrogen charging on the mechanical properties of advanced high strength

steels, Int. J. Hydrogen Energy. 39 (2014) 4647–4656. doi:10.1016/j.ijhydene.2013.12.190.

[13] L. Li, M. Mahmoodian, C.-Q. Li, D. Robert, Effect of corrosion and hydrogen embrittlement on microstructure and mechanical properties of mild steel, Constr. Build. Mater. 170 (2018) 78–90. doi:10.1016/j.conbuildmat.2018.03.023.

[14] H. Boukortt, M. Amara, M. Hadj Meliani, O. Bouledroua, B.G.N. Muthanna, R.K. Suleiman, A.A. Sorour, G. Pluvinage, Hydrogen embrittlement effect on the structural integrity of API 5L X52 steel pipeline, Int. J. Hydrogen Energy. 43 (2018) 19615–19624. doi:10.1016/j.ijhydene.2018.08.149.

[15] A. Elazzizi, M. Hadj Meliani, A. Khelil, G. Pluvinage, Y.G. Matvienko, The master failure curve of pipe steels and crack paths in connection with hydrogen embrittlement, Int. J. Hydrogen Energy. 40 (2015) 2295–2302. doi:10.1016/j.ijhydene.2014.12.040.

[16] J. Li, X. Gao, L. Du, Z. Liu, Relationship between microstructure and hydrogen induced cracking behavior in a low alloy pipeline steel, J. Mater. Sci. Technol. (2017). doi:10.1016/j.jmst.2017.09.013.

[17] R. Wang, Effects of hydrogen on the fracture toughness of a X70 pipeline steel, Corros. Sci. 51 (2009) 2803–2810. doi:10.1016/j.corsci.2009.07.013.

[18] E.V. Chatzidouros, A. Traidia, R.S. Devarapalli, D.I. Pantelis, T.A. Steriotis, M. Jouiad, Effect of hydrogen on fracture toughness properties of a pipeline steel under simulated sour service conditions, Int. J. Hydrogen Energy. 43 (2018) 5747–5759. doi:10.1016/j.ijhydene.2018.01.186.

[19] Y. Kim, Y.J. Chao, M.J. Pechersky, M.J. Morgan, On the Effect of Hydrogen on the Fracture Toughness of Steel, Int. J. Fract. 134 (2005) 339–347. doi:10.1007/s10704-005-1974-7.

[20] Y. Ogawa, H. Matsunaga, J. Yamabe, M. Yoshikawa, S. Matsuoka, Unified evaluation of hydrogen-induced crack growth in fatigue tests and fracture toughness tests of a carbon steel, Int. J. Fatigue. 103 (2017) 223–233. doi:10.1016/j.ijfatigue.2017.06.006.

[21] E. V. Chatzidouros, V.J. Papazoglou, T.E. Tsiourva, D.I. Pantelis, Hydrogen effect on fracture toughness of pipeline steel welds, with in situ hydrogen charging, Int. J. Hydrogen Energy. 36 (2011) 12626–12643. doi:10.1016/j.ijhydene.2011.06.140.

[22] J.-A. Lee, D.-H. Lee, M.-Y. Seok, U.B. Baek, Y.-H. Lee, S.H. Nahm, J. Jang, Hydrogen-induced toughness drop in weld coarse-grained heat-affected zones of linepipe steel, Mater. Charact. 82 (2013) 17–22. doi:10.1016/j.matchar.2013.05.001.

[23] M.B. Djukic, V. Sijacki Zeravcic, G.M. Bakic, A. Sedmak, B. Rajicic, Hydrogen damage of steels: A case study and hydrogen embrittlement model, Eng. Fail. Anal. 58 (2015) 485–498. doi:10.1016/j.engfailanal.2015.05.017.

[24] T. An, S. Zhang, M. Feng, B. Luo, S. Zheng, L. Chen, L. Zhang, Synergistic action of hydrogen gas and weld defects on fracture toughness of X80 pipeline steel, Int. J. Fatigue. 120 (2019) 23–32. doi:10.1016/j.ijfatigue.2018.10.021.

[25] A. Zafra, L.B. Peral, J. Belzunce, C. Rodríguez, Effect of hydrogen on the tensile properties of 42CrMo4 steel quenched and tempered at different temperatures, Int. J. Hydrogen Energy. 43 (2018) 9068–9082. doi:10.1016/j.ijhydene.2018.03.158.

[26] J. Sanchez, S.F. Lee, M.A. Martin-Rengel, J. Fullea, C. Andrade, J. Ruiz-Hervías, Measurement of hydrogen and embrittlement of high strength steels, Eng. Fail. Anal. 59 (2016) 467–477. doi:10.1016/j.engfailanal.2015.11.001.

[27] D. Hardie, E.A. Charles, A.H. Lopez, Hydrogen embrittlement of high strength pipeline steels, Corros. Sci. 48 (2006) 4378–4385. doi:10.1016/j.corsci.2006.02.011.

[28] B. Meng, C. Gu, L. Zhang, C. Zhou, X. Li, Y. Zhao, J. Zheng, X. Chen, Y. Han, Hydrogen effects on X80 pipeline steel in high-pressure natural gas/hydrogen mixtures, Int. J. Hydrogen Energy. 42 (2017) 7404–7412. doi:10.1016/j.ijhydene.2016.05.145.

[29] J.A. Ronevich, B.P. Somerday, Z. Feng, Hydrogen accelerated fatigue crack growth of friction stir welded X52 steel pipe, Int. J. Hydrogen Energy. 42 (2017) 4259–4268. doi:10.1016/j.ijhydene.2016.10.153.

[30] A. Zafra, L.B.B. Peral, J. Belzunce, C. Rodríguez, Effects of hydrogen on the fracture toughness of 42CrMo4 steel quenched and tempered at different temperatures, Int. J. Press. Vessel. Pip. 171 (2019) 34–50. doi:10.1016/j.ijpvp.2019.01.020.

[31] L.B. Peral, A. Zafra, J. Belzunce, C. Rodríguez, Effects of hydrogen on the fracture toughness of CrMo and CrMoV steels quenched and tempered at different temperatures, Int. J. Hydrogen Energy. 44 (2019) 3953–3965. doi:10.1016/j.ijhydene.2018.12.084.

[32] P. Fassina, M.F. Brunella, L. Lazzari, G. Re, L. Vergani, A. Sciuccati, Effect of hydrogen and low temperature on fatigue crack growth of pipeline steels, Eng. Fract. Mech. 103 (2013) 10–25. doi:10.1016/j.engfracmech.2012.09.023.

[33] H.B. Xue, Y.F. Cheng, Characterization of inclusions of X80 pipeline steel and its correlation with hydrogen-induced cracking, Corros. Sci. 53 (2011) 1201–1208. doi:10.1016/j.corsci.2010.12.011.

[34] H. Aydin, T.W. Nelson, Microstructure and mechanical properties of hard zone in friction stir welded X80 pipeline steel relative to different heat input, Mater. Sci. Eng. A. 586 (2013) 313–322. doi:10.1016/j.msea.2013.07.090.

[35] ASTM E1820, ASTM E1820-15 - Standard Test Method for Measurement of Fracture Toughness, ASTM International, West Conshohocken, PA, 2015. doi:10.1520/E1820-15.

[36] J.A.D. Avila, F.F. Conde, H. Pinto, J. Rodriguez, F.A.F. Grijalba, Barkhausen Noise analysis of friction stir welding of X80 pipeline steel plates (Submitted - stage: reviewing), J. Nondestruct. Eval. Barkhausen. xx (2019) xx.

[37] D. Pérez Escobar, K. Verbeken, L. Duprez, M. Verhaege, Evaluation of hydrogen trapping in high strength steels by thermal desorption spectroscopy, Mater. Sci. Eng. A. 551 (2012) 50–58. doi:10.1016/j.msea.2012.04.078.

[38] ISO 15653:2010. Metallic materials — Method of test for the determination of quasistatic fracture toughness of welds, British Standards Institution, Switzerland, 2010.

[39] J. Jiang, T.B. Britton, A.J. Wilkinson, Measurement of geometrically necessary dislocation density with high resolution electron backscatter diffraction: Effects of detector binning and step size, Ultramicroscopy. 125 (2013) 1–9. doi:10.1016/j.ultramic.2012.11.003.

[40] S. Naghdy, P. Verleysen, R. Petrov, L. Kestens, Resolving the geometrically necessary dislocation content in severely deformed aluminum by transmission Kikuchi diffraction, Mater. Charact. 140 (2018) 225–232. doi:10.1016/j.matchar.2018.04.013.

[41] A. Kumar, D.P. Fairchild, T.D. Anderson, H.W. Jin, R. Ayer, M.L. Macia, A. Ozekcin, Research progress on friction stir welding of pipeline steels, in: Int. Pipeline Conf., 2010: pp. 1–9.

[42] J.A.D. Ávila, V. Lima, C.O.F.T. Ruchert, P.R. Mei, A.J. Ramirez, Guide for Recommended Practices to Perform Crack Tip Opening Displacement Tests in High Strength Low Alloy Steels, Soldag. Inspeção. 21 (2016) 290–302. doi:10.1590/0104-9224/SI2103.05.

[43] M.R. Bayoumi, Characterization of fracture toughness of high strength low alloy steel weldments using stretch zone width measurements, J. Mater. Sci. 25 (1990) 4301–4308. doi:10.1007/BF00581088.

[44] S.I. Wright, Random thoughts on non-random misorientation distributions, Mater. Sci. Technol. 22 (2006) 1287–1296. doi:10.1179/174328406X130876.

[45] S. Zajac, V. Schwinn, K.H. Tacke, Characterisation and Quantification of Complex Bainitic Microstructures in High and Ultra-High Strength Linepipe

Steels, Mater. Sci. Forum. 500–501 (2005) 387–394. doi:10.4028/www.scientific.net/MSF.500-501.387.

[46] T. Saeid, A. Abdollah-zadeh, T. Shibayanagi, K. Ikeuchi, H. Assadi, On the formation of grain structure during friction stir welding of duplex stainless steel, Mater. Sci. Eng. A. 527 (2010) 6484–6488. doi:10.1016/j.msea.2010.07.011.

[47] M. Eskandari, M.R. Yadegari-Dehnavi, A. Zarei-Hanzaki, M.A. Mohtadi-Bonab, R. Basu, J.A. Szpunar, In-situ strain localization analysis in low density transformation-twinning induced plasticity steel using digital image correlation, Opt. Lasers Eng. 67 (2015) 1–16. doi:10.1016/j.optlaseng.2014.10.005.

[48] M.A. Mohtadi-Bonab, M. Eskandari, J.A. Szpunar, Texture, local misorientation, grain boundary and recrystallization fraction in pipeline steels related to hydrogen induced cracking, Mater. Sci. Eng. A. 620 (2015) 97–106. doi:10.1016/j.msea.2014.10.009.

[49] D.P. Abraham, C.J. Altstetter, Hydrogen-enhanced localization of plasticity in an austenitic stainless steel, Metall. Mater. Trans. A. 26 (1995) 2859–2871. doi:10.1007/BF02669644.

[50] S.K. Sharma, S. Maheshwari, A review on welding of high strength oil and gas pipeline steels, J. Nat. Gas Sci. Eng. 38 (2017) 203–217. doi:10.1016/j.jngse.2016.12.039.

[51] P. Fassina, F. Bolzoni, G. Fumagalli, L. Lazzari, L. Vergani, A. Sciuccati, Influence of Hydrogen and Low Temperature on Pipeline Steels Mechanical Behaviour, Procedia Eng. 10 (2011) 3226–3234. doi:10.1016/j.proeng.2011.04.533.

[52] J. Pak, D.W. Suh, H.K.D.H. Bhadeshia, Promoting the coalescence of bainite platelets, Scr. Mater. 66 (2012) 951–953. doi:10.1016/j.scriptamat.2012.02.041.

[53] M. Masoumi, L.P.M. Santos, I.N. Bastos, S.S.M. Tavares, M.J.G. da Silva, H.F.G. de Abreu, Texture and grain boundary study in high strength Fe-18Ni-Co steel related to hydrogen embrittlement, Mater. Des. 91 (2016) 90–97. doi:10.1016/j.matdes.2015.11.093.

[54] H.K.D.H. Bhadeshia, Bainite in Steels, 3rd ed., IOM communication Ltd, London, 2015.

[55] G. Mao, C. Cayron, R. Cao, R. Logé, J. Chen, The relationship between low-temperature toughness and secondary crack in low-carbon bainitic weld metals, Mater. Charact. 145 (2018) 516–526. doi:10.1016/j.matchar.2018.09.012.

[56] S. Lynch, Hydrogen embrittlement phenomena and mechanisms, Corros. Rev. 30 (2012) 90–130. doi:10.1515/corrrev-2012-0502.

[57] A.A.A. Saleh, D. Hejazi, A.A.A. Gazder, D.P.P. Dunne, E.V. V. Pereloma,

Investigation of the effect of electrolytic hydrogen charging of X70 steel: II. Microstructural and crystallographic analyses of the formation of hydrogen induced cracks and blisters, Int. J. Hydrogen Energy. 41 (2016) 12424–12435. doi:10.1016/j.ijhydene.2016.05.235.